ADVANCED INTELLIGENT SYSTEMS
Open Access
www.advintellsyst.com

A Novel Milli-Scale Magnetic Robot Exploiting Rotation for Controlled Magnetic Particles Release

*Giordano De Angelis, Tamerlan Srymbetov, Arianna Menciassi, and Veronica Iacovacci**

Delivering magnetic particles to specific sites in the body offers a minimally invasive approach to drug administration, enabling precise therapeutic control and reducing systemic exposure. Yet, magnetic particle deployment typically relies on invasive tools like catheters and endoscopes, which are often unsuitable for accessing complex or confined anatomical regions. This study presents a magnetically actuated milli-scale carrier capable of navigating confined environments and performing on-demand tunable release of magnetic particles across multiple release events. Particle release is achieved through a fluidic exchange mechanism triggered by the rotation of the carrier in a fluid medium. This mechanism offers the advantage of controlling the amount of particles released by adjusting the carrier rotational frequency and duration, and it proves to be efficient, releasing over 70% of the stored particles. To ensure secure transport and minimize off-target leakage, the carrier is also equipped with a flexible magnetic cap, which limits unintended leakage to below 6%. The carrier exhibits multiple locomotion modes, including drag-based locomotion, rolling, and floating, enabled by remote magnetic control. The proposed device paves the way to less invasive and more precise targeted delivery in hard-to-reach areas of the body.

1. Introduction

Traditional drug delivery methods, such as oral administration or intravenous injection, feature several complications such as poor bioavailability, lack of targeting specificity, and the risk of systemic side effects.[1,2] These limitations have fostered the search for controlled release systems capable of delivering therapeutic agents directly to targeted sites within the body.[3] In recent years, small-scale robots have emerged as a promising tool to address these challenges, offering enhanced precision and control in drug delivery applications.[4,5] Among these, magnetically driven small-scale robots have received significant attention due to their wireless actuation capabilities and high controllability.[6,7] They can move in complex environments such as viscous fluids, soft tissues, or narrow passages: this makes them ideal for navigating in complex body districts like blood vessels, the gastrointestinal (GI) tract, or lung airways.[8,9] Furthermore, external magnetic fields can be utilized to enable additional functions such as sampling,[10,11] palpation,[12] and selective drug release.[13]

Small-scale robots also offer the advantage of encapsulating and protecting therapeutic agents, shielding them from degradation caused by harsh physiological environments, such as the acidic conditions of the stomach or the action of digestive enzymes throughout the body.[14] In addition, the active movement of the robots facilitates the penetration of therapeutic agents into tissues, enhancing distribution across target regions.[15,16] This makes them interesting also for the delivery of advanced therapeutic agents such as cells,[17] gene-editing materials,[18] and magnetic micro/nanoparticles for targeted therapy.[19] The latter are highly versatile, as they can be employed for site-specific drug delivery when loaded with targeted compounds,[20] but also for inducing localized heating when exposed to external oscillating magnetic fields.[21] Magnetic particles also proved key as contrast agents in magnetic resonance imaging.[22]

However, the controlled delivery of magnetic particles presents significant challenges. First, it is essential to release particles precisely at the target site while preventing dispersion along the transport path to avoid side effects. Additionally, the number of particles released must be optimized according to their intended application and it might be beneficial to release particles in different doses at multiple locations within the target working district. A major obstacle is the tendency of magnetic cargos to aggregate or adhere to the inner surfaces of the carrier robots. More specifically, in magnetically actuated wireless carriers, the onboard magnetic elements (e.g., permanent magnets) needed for navigation can further attract and trap the particles that should be delivered, thus reducing the efficiency of their release.

Although examples of untethered carriers designed to release magnetic cargos have been reported in the state of the art,[23] these systems typically lack the ability to modulate the release in a controllable fashion. They often rely on single-shot mechanisms,[24] or on sustained continuous release through

G. De Angelis, T. Srymbetov, A. Menciassi, V. Iacovacci
The BioRobotics Institute
Scuola Superiore Sant'Anna
Viale Rinaldo Piaggio 34, 56025 Pontedera, Italy
E-mail: Veronica.Iacovacci@santannapisa.it

The ORCID identification number(s) for the author(s) of this article can be found under https://doi.org/10.1002/aisy.202500911.

DOI: 10.1002/aisy.202500911

degradation,[25] which result in a fixed amount of particles being released all at once. Moreover, traditional release mechanisms to be put on board may rely on multiple mechanical components, which add complexity and increase the risk of failure due to friction, wear, and the need for precise force balancing.[26,27] Tethered devices, on the other hand, have been employed for the delivery of magnetic cargoes,[28,29] but they are more invasive as their insertion into the body typically requires sedation or anesthesia and are featured by limited dexterity in target reaching. Table S1 in the Supporting Information compares key strategies for targeted drug delivery in the state of the art.

Achieving control over the site of release and the amount of particles delivered is a game-changing factor. This capability allows a small-scale robot to operate over time, enabling repeated use rather than being limited to a single deployment. Such functionality enhances the effectiveness of treatments requiring sustained or timed drug release while simultaneously minimizing systemic exposure.[30] Furthermore, a real-time regulation of the quantity of particles released enables small-scale robots to target multiple areas within the body and modulate therapy delivery dynamically, without the need for preprogramming specific doses. This on-demand release capability improves the precision and adaptability of treatment strategies, allowing therapeutic interventions to be tailored in response to the specific needs of the body environment or to external stimuli.

In this work, we present a novel magnetic milli-scale carrier (MSC) capable of releasing magnetic particles in a controlled amount by exploiting its own rotation. We show that the MSC rotation in a fluid triggers the release of particles stored in its internal cavity and that rotation duration and frequency act as control parameters over release. The carrier features also a hard-magnetic soft deformable cap that enables at the same time safe transport of magnetic particles while navigating and on-demand release. In light of its compact size, the MSC can be orally ingested and can be controlled through different locomotion modes such as rolling, floating, and dragging under a remote magnetic field. The unique features of this device pave the way for more efficient and less invasive magnetic particle delivery, with potential applications in biomedical diagnostics and treatments.

2. Results

2.1. Concept and Working Principle of Magnetic Milli-Scale Carrier for Controlled Particle Release

In **Figure 1**A an overview of the MSC realized for the targeted release of magnetic particles and eligible for operation in the GI tract is illustrated. The system is remotely actuated by an external magnetic field and designed to enable both localized delivery and precise control over the amount of magnetic particles released.

The MSC consists of a cylindrical body with a coaxial internal cavity devised to store a magnetic cargo, specifically a suspension of magnetic particles (Figure 1B). The MSC includes two soft permanent magnets: a magnetic plate that stands on the rear part of the body, enabling MSC navigation and controlled release under remote magnetic guidance; and a magnetic cap attached to the MSC front face to ensure that the internal cavity remains sealed during navigation. Both the plate and the cap consist of a silicon NdFeB composite (see MSC Design and Fabrication in the Experimental Section), whereas the cylindrical body is 3D-printed using polyethylene terephthalate glycol (PETG). The magnetic plate possesses a diametrical magnetization M_1 while the cap features an axial magnetization M_2. The MSC is designed to be smaller than a double-zero capsule dimension,[31] being 12 mm in length and 8 mm in diameter (Figure 1C).

The operating principle of the MSC is illustrated in Figure 1D. During navigation, the cap remains closed while the carrier moves under magnetic guidance. Once the target area is reached, a stronger magnetic field is applied to exceed a critical threshold B_c and let the cap open. Subsequently, a rotating magnetic field produces MSC synchronous rotation and triggers fluid exchange between the internal cavity of the carrier and the external environment, resulting in the release of the stored particles. The quantity of released particles can be modulated by controlling the rotational frequency of the carrier and its rotational duration.

The proposed rotation-induced mechanism depends on hydrodynamics at the robot-fluid interface. The MSC can therefore release both magnetic and nonmagnetic payloads provided they are suspended in the cavity fluid. Figure S9 in the Supporting Information shows the delivery of different nonmagnetic payloads (food dyes, polystyrene beads, and inorganic particles), demonstrating that the release mechanism is transversal to different cargo types and sizes.

The MSC demonstrated efficient performance in aqueous environments by releasing more than 70% of magnetic particles stored inside its cavity, while maintaining minimal losses during navigation by applying a low magnetic field control. Moreover, the MSC proved capable of multimodal locomotion at the air–water interface, in confined environments and in fluids with different viscosities employing both gradient-based drag and rolling locomotion.

2.2. Numerical Analysis

Numerical simulations were conducted to guide the design of the release mechanism. In particular, simulations helped to build dependencies between flow regimes, force ranges, and carrier design variables (e.g., cavity size and distance from the magnetic plate). Finite element method (FEM) analysis (COMSOL Multiphysics) was adopted for this purpose.

Numerical simulations revealed that when the carrier rotates in a fluid medium, shear forces are developed along its walls, leading to the formation of coherent vortices. As expected, given that the MSC features a deep cavity, defined by a length-to-diameter ratio greater than 2, a single primary vortex forms near the cavity end during rotation.[32] This shear-driven vortex facilitates fluid exchange between the cavity and its surrounding medium,[33] contributing to cargo release. When fixing the cavity size (diameter and length 2 and 6 mm, respectively), it was found that the carrier rotating frequency has a direct effect on the flow profile (**Figure 2**A–C): the higher the frequency, the higher the flow velocity around the carrier and inside the cavity.

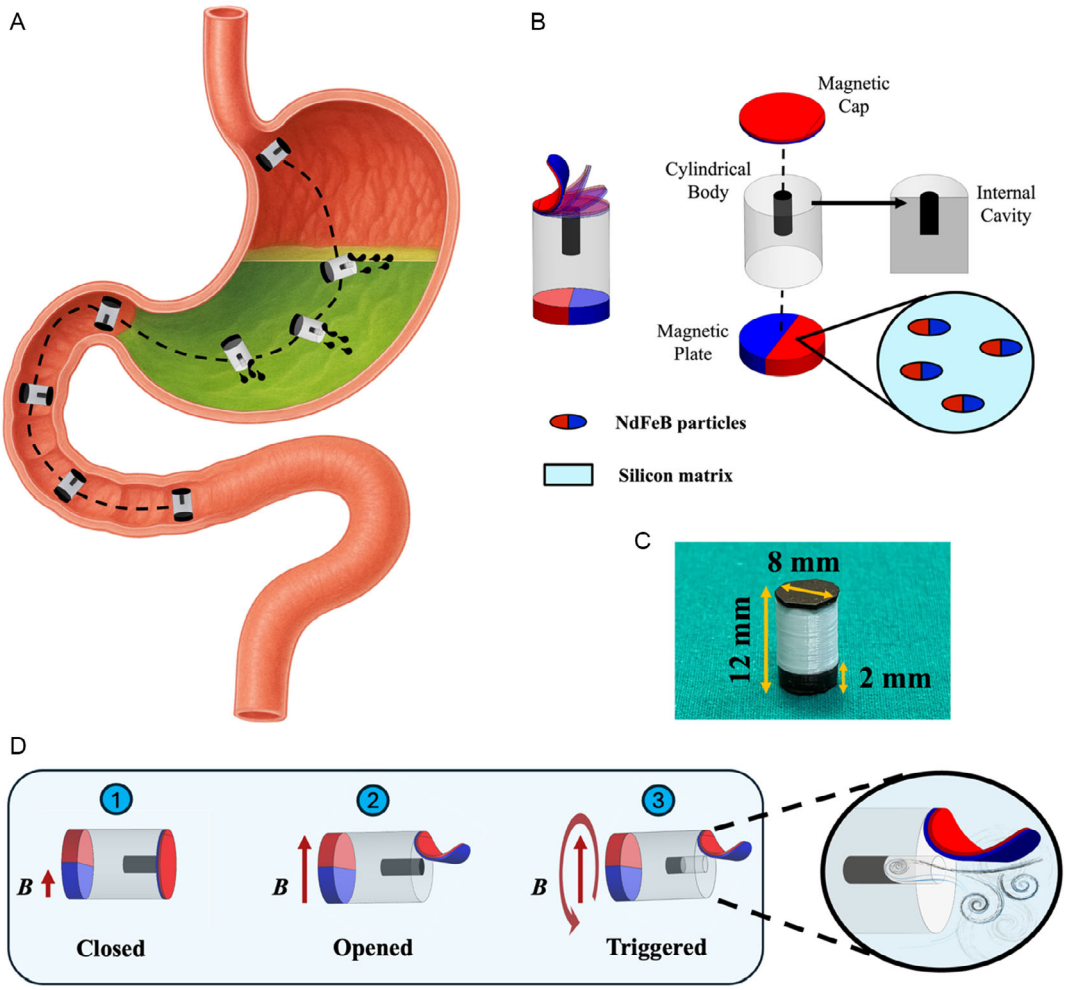

Figure 1. Milli-scale carrier design and working principle. A) Concept of the milli-scale carrier (MSC) navigating through the gastrointestinal tract and releasing particles within the stomach. B) Illustration of the MSC characterized by a cylindrical geometry with an internal cavity for cargo storage. The carrier features a magnetic cap to prevent cargo loss and a magnetic plate for actuation. C) Optical image of the MSC prototype. D) Illustration of the release mechanism of the carrier. By applying a rotating magnetic field, the carrier rotates activating an exchange of fluid between the internal cavity and the workspace, thus triggering the release of particles.

When looking at the x component of flow velocity inside the cavity (Figure 2D–F), the profiles suggest stable inflow ($v_x^{cav} < 0$) and outflow ($v_x^{cav} > 0$), especially close to the end of the cavity, which can be interpreted as stable fluid exchange. In this regard, we studied the fluid outflow rate from the cavity to the surrounding medium and examined its dependence on two control parameters: the cavity diameter and the carrier rotation frequency (Figure 2G). On the graph, it is evident that a larger cavity diameter increases the fluid exchange between the cavity and the outer environment. Specifically, for cavity diameters larger than 1 mm, the outflow rate increases at a higher rate with frequency if compared to smaller diameters.

To enable the release of magnetic particles stored inside the cavity, the drag force F_d generated by the fluid exchange during rotation must exceed the magnetic attraction force F_m produced by the magnetic plate over the particles. By neglecting the effect of gravity, F_d and F_m can be combined to find a critical escape velocity v_{escape} and the corresponding critical distance d_c at which the particles can escape the field generated by the magnetic plate. Here, we studied the magnetic attraction force F_m between the plate (having a magnetization M_1 of 200 kA m^{-1}) and NdFeB particles when varying particles distance from the plate. In the simulation setup, we assumed that the magnetic field produced by the magnetic plate is not strong enough to promote clustering of the particles. Therefore, calculations of v_{escape} were performed for a single particle.

Results (Figure 2H) show how v_{escape} varies as a function of the distance from the magnetic plate for different particle sizes. We can observe that larger particles exhibit higher escape velocities: magnetic force increases fast with volume, while drag force increases more slowly proportionally to the cross-sectional area. Given typical flow velocity values obtained from simulations (Figure 2D–F), our findings support the feasibility of releasing particles with a diameter smaller than 10 μm at distances from the magnetic plate larger than 4 mm. For larger magnetic objects, the cavity length and overall carrier dimensions should be adjusted to optimize particle release.

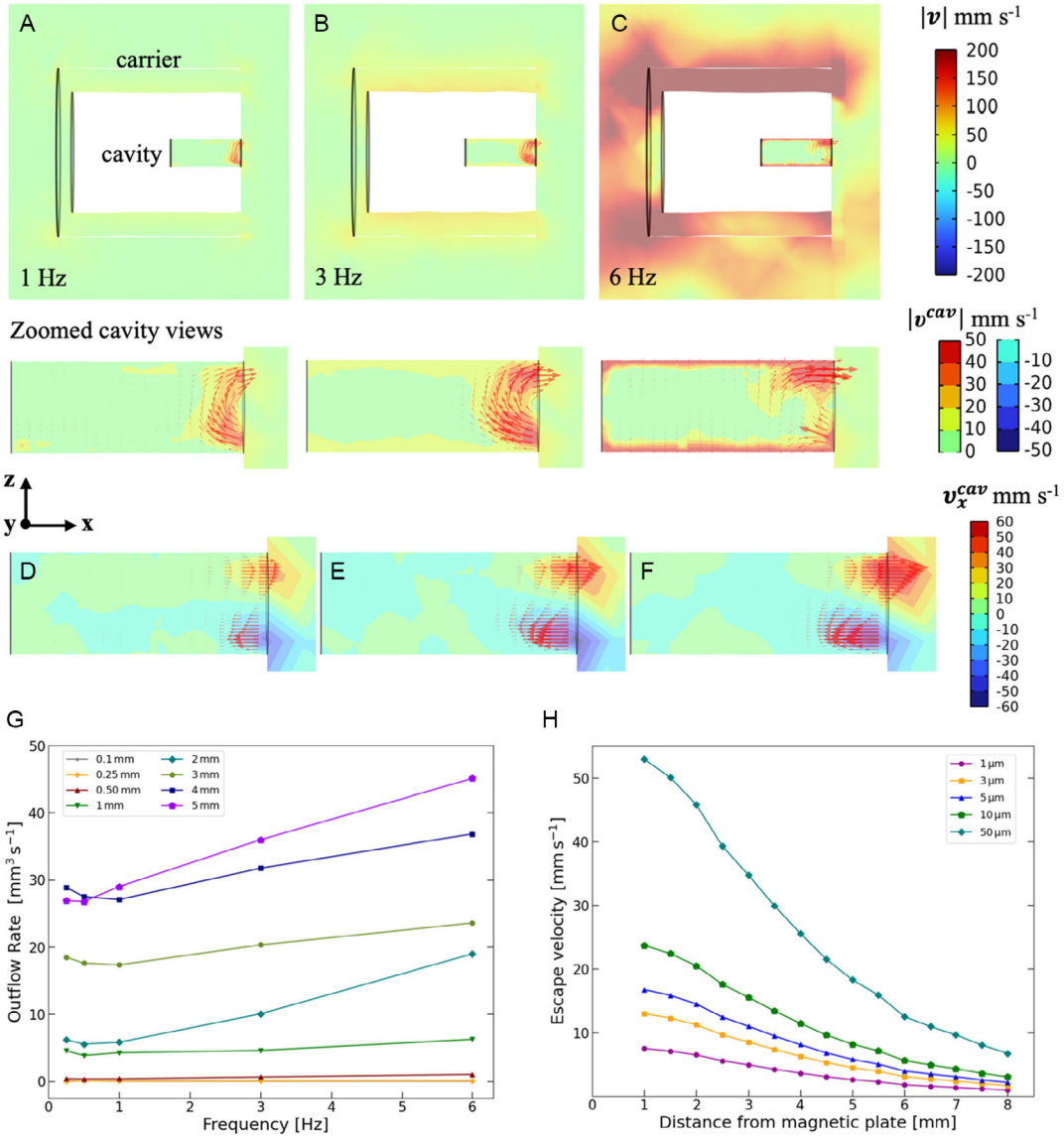

Figure 2. Numerical simulation of the flow field generated by the MSC rotation. Fluidic simulations showing the flow velocity profile around the carrier and inside the cavity during the rotation at different frequencies: A) 1 Hz, B) 3 Hz, and C) 6 Hz with a common legend shown on the right. The flow velocity *x* component profile inside the cavity when the carrier rotates at different frequencies: D) 1 Hz, E) 3 Hz, and F) 6 Hz. G) Outflow rate dependency on cavity diameter and the rotating frequency. H) Study of the critical escape distance and flow velocity for different diameters of NdFeB particles.

For instance, since we want the particles to consistently escape the carrier, the cavity must be positioned at a distance from the plate greater than the critical distance, where the magnetic influence is minimal. This allows the particles to exit the cavity even at low fluid velocities. Being l_c the length of the cavity and t_{plate} the thickness of the magnetic plate, the total length of the carrier can be expressed as $L = t_{plate} + d_c + l_c$. Thus, the cavity length can be determined according to the critical distance d_c (see Figure S3 in Supporting Information).

It is important to note that, due to its small volume and relatively low magnetization (approximately four times lower than that of the magnetic plate), the cap does not generate a sufficient magnetic force to influence particle release. In fact, the magnetic attraction force exerted by the cap over the particles is at least two times weaker than both the gravitational and drag forces acting on them during release.

To characterize the release dynamics, we evaluated the coupling between the carrier-induced flow and the NdFeB particles via the Stokes number St. If $St \ll 1$, particles are expected to follow the local fluid streamlines. For rotation frequencies up to 6 Hz and the particle sizes used in this study, we obtained $St < 0.01$, indicating negligible particle inertia.

On this basis, we performed particle tracing simulations for NdFeB particles with diameters of 1, 5, 10, and 50 µm. Results are reported in Figure S2 and Movie S1, Supporting Information. After leaving the cavity, particles follow the outward flow and form a dispersed cloud that is transported away from the carrier by viscous drag. For particle sizes within the $St \ll 1$ range

relevant to our experiments, the release does not occur as a single compact cluster, but rather as a continuous or weakly modulated stream of particles that rapidly spreads into the surrounding fluid.

Overall, our model treats NdFeB particles individually, without considering agglomeration, which represents a simplifying yet physically reasonable assumption. This is consistent with experimental and theoretical findings. Magnetic microparticles generally require fields above 100 mT to initiate aggregation.[34] The simulations indicate that the particles are exposed to a maximum magnetic field of 7 mT when accounting for both the plate and the cap. Although a 7 mT field may induce some degree of interparticle attraction, the combined effects of carrier motion and spatial nonuniformity of the applied field are expected to prevent significant clustering and preserve the release process.

2.3. Magnetic Cap Characterization

To ensure that the MSC can navigate dexterously and with different locomotion modalities while preventing unintended particle loss, we developed a magnetic mechanism featuring a hard-magnetic soft deformable cap that allows the carrier to operate in two configurations: open and closed. This mechanism relies on the balance between the elastic restoring torque T_e that acts to keep the cap closed and the externally applied magnetic torque T_m that tends to open it.

As shown in **Figure 3**A, when an external magnetic field B is applied along the z-axis, the magnetic plate experiences no torque, as its magnetization M_1 is aligned with B. On the other hand, the cap with a magnetization M_2 perpendicular to M_1 experiences a torque T_m and tends to align with the external magnetic field. If T_m exceeds T_e, the cap begins to open, rotating of a certain angle around its hinge point. To capture this behavior, we use a simplified model in which the cap elastic restoring torque is represented by a linear torsional spring under a small-angle approximation, being

$$|T_m| = |T_e| = |m_2 \times B| = k|\theta| \tag{1}$$

where $m_2 = M_2 V_2$ is the magnetic moment of the cap with a volume V_2, k is the torsional stiffness of the cap, and θ is the angle between the cap and the front face of the carrier. We can approximate the behavior of the cap as the cantilever beam model, treating it as a linear elastic solid with constant Young modulus E and assuming a uniformly distributed moment. For a slender cantilever undergoing small deflection, the rotational stiffness scales as $k \approx EI/L$, thus we have

$$m_2 B \sin \alpha = \frac{EI}{L}\theta \tag{2}$$

where I is the moment of inertia and L is the length of the cap. We can rewrite the equation noting that α is complementary to theta

$$m_2 B \cos \theta = T_0 + \frac{EI}{L}\theta \tag{3}$$

Here we add a torque barrier T_0 to account for the effect arising from Coulomb friction and surface adhesion at the cap–carrier interface.

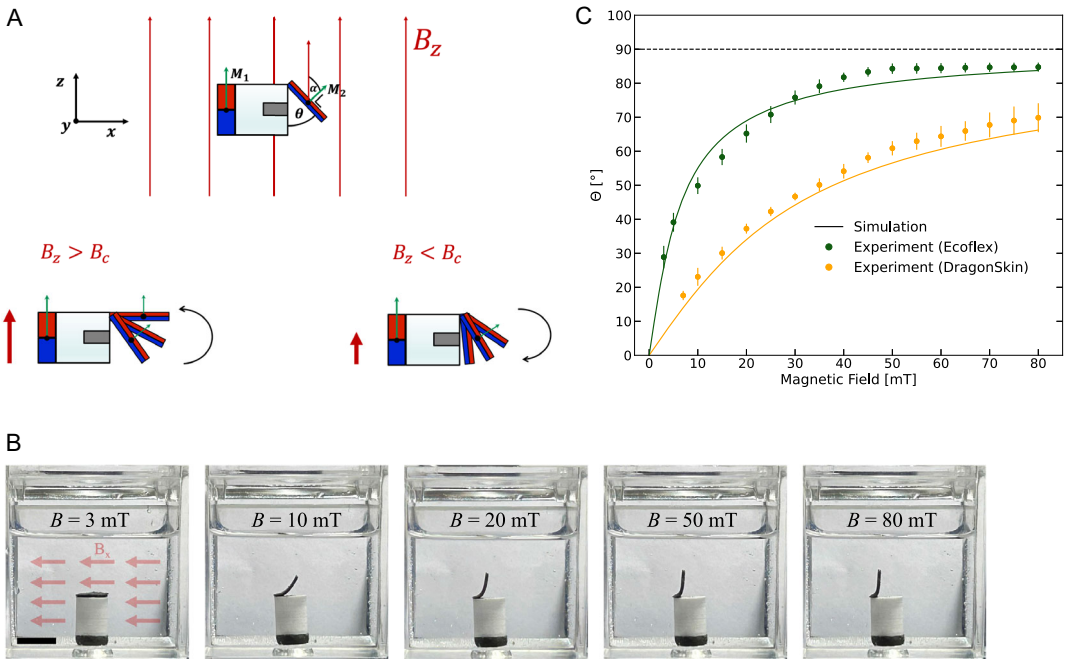

Figure 3. Open/close mechanism working principle and magnetic cap characterization. A) Illustration of the working principle of the open/close mechanism of the magnetic cap. As the magnetic field increases, the cap begins to open, while it remains closed when the applied magnetic field is below a certain threshold value. B) Snapshots of the Ecoflex cap opening mechanism under increasing applied magnetic field. Scale bar: 10 mm. C) Opening angle plotted against the applied magnetic field for both Ecoflex 00-10 and Dragonskin 00-10 composite caps. Each data point represents the mean value over five samples, while the full line corresponds to the results of the numerical simulation.

From (3), we can see that the opening angle θ depends on the applied magnetic field B. Thus, we can define a critical magnetic field value B_c acting as a threshold. In the limit as $\theta \to 0$, $\cos\theta \to 1$, this relation yields a practical estimate of the critical field: $B_c \approx T_0/m_2$. For $B < B_c$ the cap stays closed preventing particle loss, whereas for $B > B_c$ the cap opens, with θ approaching 90° as B increases. Therefore, to guarantee that the carrier remains closed during navigation, it is crucial that the magnetic field during navigation does not exceed B_c. Additionally, to achieve efficient particle release, it is essential to identify the magnetic field that ensures an optimal cap opening.

We adopted this simplified model because it helps describing intuitively the magnetic and elastic torque balance with a reduced number of parameters and yields a clear design rule separating navigation (closed cap) from release (open cap). However, this model provides good quantitative outputs only in the small-angle regime ($\theta \lesssim 20°$) and neglects shear deformation and viscoelastic phenomena. For a more complete description at large angle, we employed a semiempirical elastic torque-angle law (see Magnetic Cap Characterization in the Experimental Section).

To precisely control the opening and closing mechanism and optimize the design of the carrier, we characterized the cap behavior for two materials with different mechanical properties. Specifically, we compared the performance of an Ecoflex 00–10 cap embedded with 40% of NdFeB microparticles to that of a Dragonskin 00-10 cap with the same particle composition. The Ecoflex cap has a Young's modulus of 73 kPa, while the Dragonskin cap exhibits a Young's modulus of 336 kPa. Both materials have comparable remanent flux density, measured at 0.113 T (please refer to Magnetic Cap Characterization in the Experimental Section for details).

Figure 3B shows representative images used for the characterization process. The MSC equipped with the Ecoflex cap is placed at the bottom of a cubic workspace filled with water. A uniform magnetic field is applied along the x-axis. In this configuration, the magnetic moment of the plate is aligned with the field, while the magnetic moment of the cap experiences a magnetic torque due to its misalignment with it. Distinct cap opening configurations can be observed depending on the intensity of the applied magnetic field. Notably, at a field strength of ≈3 mT, the cap remains closed, while an applied field of 50 mT results in an almost fully open configuration.

Figure 3C displays the measured opening angles for both the Ecoflex and Dragonskin caps as a function of the applied magnetic field (range 0–80 mT). Our measurements show that beyond a certain magnetic field strength, ≈40 mT for the Ecoflex cap and 55 mT for the Dragonskin cap, the opening angle reaches a saturation point. This behavior defines the range of magnetic field intensities required to achieve an optimal opening for an efficient release. Additionally, we observed that the cap remains closed when the applied magnetic field is below 7.2 ± 0.6 mT for the Dragonskin cap and 4.1 ± 0.4 mT for the Ecoflex cap. Accordingly, these values can be considered as the opening threshold magnetic fields. The experimental data show good agreement with the predictions of the introduced beam model, with a global R-squared value of about 90% for both materials. Most of the discrepancies that are observed from the simulation can be attributed to the fact that we adopted a semiempirical model (see Experimental Section) that neglects distributed magnetic loading along the soft cap and relies on the accuracy of the calibrated data. More accurate and complex models can also be adopted to simulate the nonlinear magnetoelastic behavior of the cap, such as neo-Hookean rod models,[35] Kirchhoff/Cosserat models,[36] finite-element magnetoelastic formulations,[37] or even closed-form large-deflection solutions.[38]

As expected, for the same applied magnetic field, the Dragonskin cap exhibits a smaller opening angle, indicating that increased stiffness inhibits cap deformation. Therefore, a more rigid cap is preferable, as it ensures that the MSC remains closed at higher magnetic field intensities, allowing better navigation control and a more secure sealing mechanism.

2.4. Characterization of Milli-Scale Carrier for Controlled Magnetic Particles Release

To evaluate the release performance of the MSC, we tested 20 MSC prototypes and studied their behavior in a controlled experimental setting. As illustrated in **Figure 4**A, the MSC is positioned at the bottom of a water-filled container. When a relatively small magnetic field is applied along the z-axis (3 mT), the magnetic plate on the rear aligns with the applied field while the magnetic cap remains closed. Upon increasing the magnetic field magnitude (60 mT), the cap opens. At this stage, by applying a continuously rotating magnetic field on the zy-plane, the carrier synchronously rotates with the field, thus triggering the release of the stored particles (Movie S2, Supporting Information). The quantity of released particles can be modulated by controlling the rotational frequency and duration of the carrier. To characterize this release mechanism, we conducted a series of experiments in which both the rotation frequency of the carrier and the duration of rotation were systematically varied.

In the first set of experiments, we investigated how the release efficiency, defined as the percentage of particles released relative to the total amount of particles stored in the cavity, varies with rotational frequency (range 0.25–6 Hz, $B = 60$ mT, test duration 20 s). Experiments were performed using two prototype designs, one equipped with the magnetic cap (labeled as Cap) and one without it (labeled as Open). As expected from the simulations, release efficiency increased with increasing rotational frequency (Figure 4B). For example, considering the Open prototype, at 0.25 Hz rotational frequency, ≈25% of the particles were released. Between 0.25 Hz and 1 Hz, the release percentage rose to about 45%, and in the higher frequency range of 3 to 6 Hz, it rose further to ≈60%. The percentage of particles released for both prototypes follows a similar trend, with statistically significant differences observed only at 3 and 6 Hz ($p < 0.05$, 2-tailed t-test), where the Open carrier demonstrated higher release efficiency.

Notably, when the carrier is stationary (0 Hz) with an open cap, a small percentage of particle release occurred. This spontaneous release, ≈10%, could be attributed to natural fluid exchange between the cavity and the surrounding environment.

The duration of the release event proved to be another interesting control parameter over the delivered cargo amount. As shown in Figure 4C, an increase in rotational time resulted in

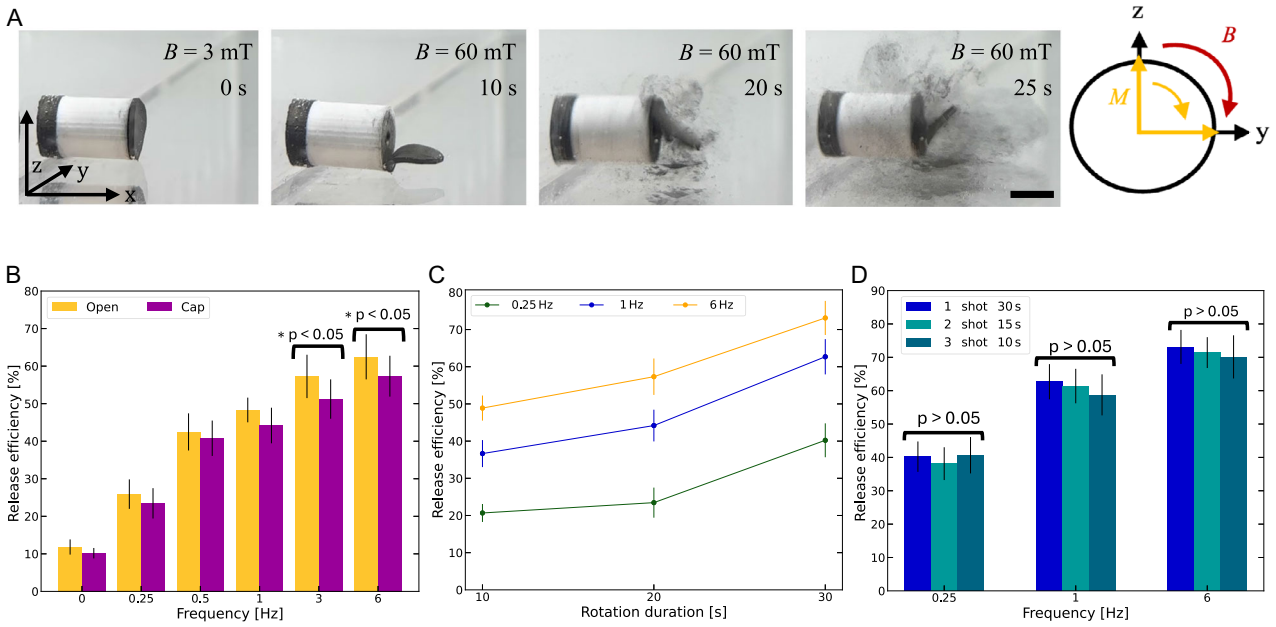

Figure 4. Characterization of magnetic particle release. A) Optical images of the MSC before and after the release process. Initially, the magnetic cap is closed. When a 60 mT magnetic field is applied along the z-axis, the cap opens, and then by applying a 1 Hz rotating magnetic field on the *zy*-plane, the carrier starts to rotate, releasing magnetic particles. Scale bar: 5 mm. B) Particle release efficiency as a function of the carrier rotational frequency for both Open and Cap prototypes. C) Particle release efficiency when varying the rotational frequency and rotation duration of the carrier. D) Particle release efficiency when varying the number of release events over the same rotation period.

a higher percentage of particles being released. Here, as in the following section, we are considering tests carried out with the Cap prototype. Crucially, controlling both the release duration and the rotational frequency significantly enhances the versatility of the MSC, allowing precise regulation of cargo release even in conditions where frequency control is constrained, such as high-friction environments that impose a low step-out frequency.

Results demonstrated that at a high frequency and duration of the rotation of the MSC achieves a greater release efficiency, reaching its maximum at $73.1 \pm 4.6\%$ for a total rotation time of 30 s at 6 Hz. This peak indicates a moderate-to-high release efficiency, suggesting that the carrier effectively enables magnetic particle delivery in aqueous environments. The remaining fraction of unreleased particles is attributed to internal surface effects, as some particles adhere to the inner walls of the cavity.

To further characterize the controlled release, we also investigated how the number of release events, i.e., the triggers initiating and stopping the carrier rotation, affects the amount of particles released when keeping the overall rotation duration constant. Figure 4D presents the experimental results for the MSC actuated at 0.25, 1, and 6 Hz. For each frequency, we analyzed three conditions: a single 30-s release event, two 15-s release events, and three 10-s release events. No statistically significant difference was observed when varying the number of release events ($p > 0.05$). This suggests that the MSC can consistently release particles across multiple events, enabling a repeatable, controlled release in different target areas.

Lastly, to assess the sealing capability of the magnetic cap, we conducted both static and dynamic measurements of spontaneous particle loss (Figure S7, Supporting Information). In the static scenario, the carrier was immersed in water for an extended period of 48 h without the application of any external magnetic field. The results indicate good sealing performance, with the spontaneous release remaining stable at $3.8 \pm 0.7\%$. In the dynamic scenario, specifically during carrier floating and rolling (see Section 2.5 for details on MSC locomotion), the percentage of particle loss was $4.2 \pm 0.8\%$ in floating mode and slightly higher, namely $5.4 \pm 0.7\%$, during rolling. These results demonstrate that the magnetic cap effectively limits particle loss, thereby preserving the intended cargo for release and reducing toxicity risks.

2.5. Multimodal Locomotion Control in Different Environments

When considering potential applications in the GI tract, the MSC has to withstand a variety of environments characterized by confined spaces with sharp curvatures, uneven terrains with obstacles, and fluid regions with various viscosities. These complex conditions require precise magnetic actuation and accurate external field control to achieve stable, adaptive, and safe navigation. Here we demonstrate that the proposed MSC is capable of multiple locomotion modes, including floating at the air-water interface, rolling underwater and in viscous media (e.g., glycerol), and drag-based locomotion within narrow spaces (e.g., a tube). Multimodal locomotion can be achieved using an external magnetic field generated by a permanent magnet that exerts a gradient pulling force and a torque on the MSC.

In the first scenario, a floating configuration at the air–water interface was achieved, as shown in **Figure 5**A. This equilibrium is established when the magnetic force F_m generated by a

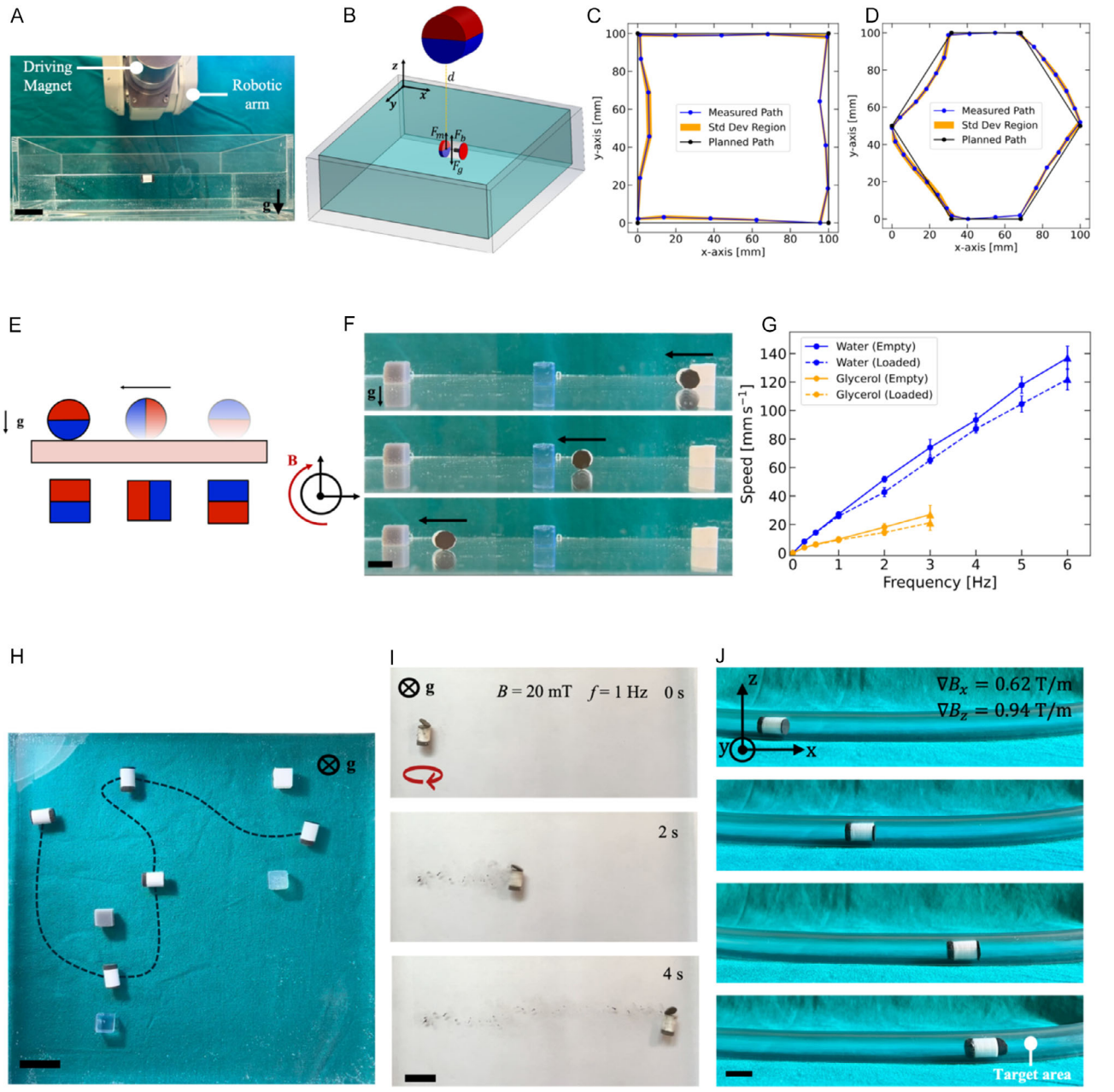

Figure 5. Magnetic control of the MSC and multimodal locomotion. A) Optical images of the experimental setup demonstrating the MSC control in a floating configuration. Scale bar: 20 mm. B) Illustration of the forces involved in floating locomotion. C) Hexagonal and D) rectangular path tracking analysis of the MSC in floating locomotion. The black line represents the planned trajectory provided as input to control the robotic arm. E) Illustration of the rolling locomotion actuation. F) Snapshots of the MSC rolling in water by applying a rotating magnetic field of 5 mT at 1 Hz. Scale bar: 10 mm. G) Translational speed of the carrier in water and glycerol when varying frequency, triangles indicate the relative step-out frequency. H) Snapshots of the MSC following a complex trajectory via steering locomotion underwater. Scale bar: 20 mm. I) Snapshots of the MSC releasing magnetic particles while rolling underwater under a 20 mT rotating magnetic field applied at a frequency of 1 Hz. Scale bar: 15 mm. J) Optical images of the MSC navigating through a 10 mm-diameter tube via magnetic drag locomotion, while maintaining the cap closed. The magnetic cap is opened upon reaching the target area. Scale bar: 10 mm.

permanent magnet, together with the buoyant force F_b, counterbalances the gravitational force F_g acting on the MSC (Figure 5B). There is a specific range of magnetic forces that allows the carrier to reach a state of floating equilibrium, as determined by the following condition on the vertical components of the forces: $F_g - F_b < F_m < F_g$. We assessed experimentally that the carrier can float for applied magnetic fields above 2 mT, which corresponds to a maximum distance between the magnet and the carrier of ≈14 cm. In this configuration, the carrier can navigate on the *xy*-plane defined by the water surface, while its position and orientation are precisely controlled by controlling the magnet through a robotic arm.

The magnetic field applied to achieve the floating equilibrium is below the safety threshold of 7 mT required to keep the magnetic cap closed. Consequently, the carrier can navigate safely while keeping the cap sealed.

Additionally, we evaluated the accuracy with which the MSC followed a predefined trajectory in the floating configuration. The carrier was tested on both a rectangular (Figure 5C) and a hexagonal (Figure 5D) path. This control has demonstrated precision and repeatability, as the maximum standard deviation on the average path was found to be 13.6% of the body length for the rectangular path and 16.4% for the hexagonal path. The observed deviations from the planned trajectory (black line) are primarily attributed to the movement constraints of the robotic arm imposed by its joint limits.

In the second scenario, we demonstrate the carrier ability to move across different media through rolling motion. As illustrated in Figure 5E, the carrier can be propelled on a flat surface by applying a continuous rotating magnetic field generated by a driving magnet. The driving magnet exerts a pulling force that presses the MSC on the surface, ensuring the presence of enough friction to achieve rolling. At the same time, the rotating magnetic field generates a torque on the carrier, allowing it to roll continuously. Figure 5F provides a visualization of this functionality, showing the carrier to perform rolling locomotion underwater, driven by an external rotating magnetic field with a magnitude of 5 mT at a frequency of 1 Hz.

We further investigate how the rolling motion velocity varies as a function of rotational frequency for both an empty and a loaded carrier in water and glycerol (Figure 5G). In water, the MSC exhibits pure rolling locomotion with speeds ranging from 8 to 136 mm s^{-1} as the frequency varies from 0.25 to 6 Hz. In glycerol, the carrier demonstrates a combination of rolling and slipping motion, with velocities ranging from 4 to 26 mm s^{-1} as the frequency varies from 0.25 to 3 Hz. The upper frequency limits of 6 Hz (in water) and 3 Hz (in glycerol) correspond to the step-out frequencies of the carrier under a 5 mT rotating magnetic field, beyond which it loses synchronous rotation with the field. Our findings indicate that even when the applied magnetic field remains below the critical threshold to maintain the cap closed, the MSC can still move effectively in aqueous environments or even in higher viscosity media such as glycerol.

In Figure 5H, we demonstrated the carrier ability to follow a complex trajectory through steering locomotion. The carrier is immersed in water within a cubic box containing some obstacles. The driving magnet, mounted on the robotic arm with its last joint free to rotate, is positioned below the tank (Figure S5B, Supporting Information). By controlling the plane of rotation of the driving magnet we achieved dexterous control of the carrier as it moves through the obstacles (Movie S3, Supporting Information). These results demonstrate that the proposed control method is effective for navigating tortuous environments that require complex maneuvering to avoid obstacles and perform sharp turns.

The MSC unique design also allows the release of particles while rolling. During rolling locomotion, if a magnetic field strong enough to open the cap is applied, the rotation of the carrier will trigger fluid exchange between the internal cavity and the external environment, leading to the release of particles (Figure 5I). When the carrier rotates, the amount of particles released can be controlled by adjusting its frequency and duration, as shown in Section 2.4. This capability offers several advantages, such as increased dispersion across tissue volume, since the carrier can spread particles more effectively compared to static release, thereby improving bioavailability. Moreover, motion-driven release enables spatially distributed dosing, with the release rate adapting to the location of the carrier within the environment.

In the third scenario, we demonstrated that the MSC can be actively locomoted in a confined space using the dragging force generated by an external permanent magnet while maintaining the cap closed (Figure 5J). The carrier was placed inside a tube with an internal diameter of 10 mm. By translating the external magnet along the tube at velocities up to 10 mm s^{-1}, a spatially varying magnetic field gradient was generated, producing a net drag force that pulls the carrier forward (Figure S11, Supporting Information). Here, we quantified the minimum magnetic gradient required to overcome static friction and initiate locomotion, resulting in a value of 1.04 ± 0.5 T m^{-1}. These results confirm the capsule effective navigation, responsive control under relatively small magnetic force, and demonstrate its capability to operate in constrained environments with elevated wall-induced friction.

3. Conclusion

The targeted release of magnetic particles within the body represents a potentially revolutionary technique, enabling the delivery of therapeutic agents directly to the desired site while minimizing complications associated with systemic toxicity. However, magnetic particles must be protected from the harsh physiological environment during navigation and released in a controlled manner at the target site to ensure therapeutic efficacy. Conventional delivery methods, such as catheters and endoscopes, are limited in their ability to access confined or anatomically complex regions and are inherently invasive, as they involve deep insertion through the body, causing discomfort and frequently requiring sedation or anesthesia. Untethered capsules have emerged as less invasive alternatives, but they are typically constrained by a fixed payload capacity, limiting the ability to modulate the quantity of released particles. As a result, multiple administrations are often necessary to treat multiple target areas.

Here we reported a MSC for targeted release of magnetic particles that can tune the amount of particles released based on its rotational frequency and duration. The carrier can be fully controlled by applying external magnetic fields to allow precise navigation and on-demand release of magnetic particles.

We showed that the carrier is capable of releasing magnetic particles exploiting a fluid exchange mechanism triggered by its own rotation. Our approach focused on studying this mechanism and optimizing the carrier design to facilitate cargo release. To this end, we performed fluidic and magnetic simulations to investigate the behavior of the carrier during rotation in a fluid and to properly dimension the MSC to guarantee efficient operation.

The carrier features an open/close mechanism designed to ensure the secure storage of particles during navigation.

We demonstrated that this solution effectively minimizes particle leakages during various locomotion modes, with total particle loss remaining below 6% of the initial amount stored in the cavity. Additionally, experimental results confirmed that the presence of the magnetic cap does not compromise the carrier ability to release magnetic particles, as the release performance is comparable to that of the prototype without the cap.

We systematically investigated the carrier ability to release particles, demonstrating its effectiveness in controlling the release quantity by tuning its rotational frequency and rotation duration. Furthermore, we showed that the MSC is capable of releasing particles across multiple events, enabling repeatable and controlled delivery at different target sites. The system proved to be efficient by releasing more than 70% of the total particles stored in its internal cavity.

Compared to existing state-of-the-art prototypes, the proposed MSC can efficiently release magnetic particles while enabling on-demand control over the release quantity. This feature allows the administration of a nonpredefined dose, allowing real-time adaptation to specific clinical needs. At the same time, it helps minimize the number of administrations required, as a single carrier can perform multiple releases at distinct target sites.

Several aspects of the MSC can be improved. First, reducing the size of the capsule could enable targeting less accessible regions of the GI tract or other parts of the body, where localized delivery of magnetic particles may be particularly beneficial. Miniaturization would expand the range of clinical applications, allowing for therapeutic intervention in anatomically constrained or sensitive areas. At the same time, the opening design could be further optimized to improve both the robustness and efficiency of release. For example, multiple or circumferential openings could be introduced to reduce orientation-dependent bursts and promote a smoother spatial distribution, or a flow-restricting outlet could be integrated to damp rapid cavity-environment exchange and enable a more gradual release.

Second, to validate the efficacy and safety of the MSC in a realistic physiological environment, it is essential to perform tests in fluids that mimic those present in the GI tract. These tests would provide critical insights into the carrier's resistance to acidic conditions, enzymatic degradation, and its ability to release active compounds in non-Newtonian fluids.

Third, to enhance the precision of particle delivery and navigation, the implementation of a closed-loop control system could be explored. For instance, integrating real-time localization methods, such as ultrasound imaging, with robotic actuation would allow for dynamic feedback-based control of the MSC's position and release.

Finally, due to its simple structure and internal space availability, the MSC can potentially be integrated with additional functional units. These could include onboard sensing components capable of detecting specific physiological or pathological markers (e.g., pH changes, enzyme concentrations, or temperature variations) to precisely localize and confirm the intended delivery site prior to release. Alternatively, multiple compartments could be designed to carry and selectively release different types of therapeutic agents, not limited to magnetic particles. Such multifunctionality would further expand the utility of the system in complex therapeutic scenarios.

4. Experimental Section

MSC Design and Fabrication: The proposed MSC was fabricated using a combination of manufacturing techniques and assembled manually in the laboratory. The cylindrical body of the prototype was 3D-printed using PETG.

The magnetic components, namely the plate and the cap, were created by blending silicone with NdFeB magnetic microparticles (average size 5 μm; Magnequench, USA) to form a uniform composite. The magnetic plate was fabricated by mixing Ecoflex 00-10 (Smooth-On Inc., USA) with 60% w/w magnetic microparticles. The magnetic cap was produced according to the same protocol while incorporating 40% w/w of magnetic microparticles into either Ecoflex 00-10 or Dragonskin 00-10. These mixtures were poured into 3D-printed molds, cured, and subsequently permanently magnetized, using an impulse magnetizer (T-series, MAGNET-PHYSIK, Germany).

The magnetic plate, attached to the rear part of the cylinder, has a thickness of 2 mm and was diametrically magnetized. The magnetic cap, positioned at the front of the main body, has a thickness of 0.5 mm and an axial magnetization. Both the plate and cap were attached to the main body using cyanoacrylate glue. Notably, the magnetic cap was precisely attached to the front face of the carrier at a designated hinge point, the one corresponding to the north pole of the magnetic plate, to ensure that the cap opens when a magnetic field exceeding the critical threshold is applied (Figure 1B).

Simulation and Modeling: Numerical simulations were performed in COMSOL Multiphysics. Major modeling elements and simulation workspace of fluid dynamics simulations are displayed in Figure S1, Supporting Information. The schematic of the rotating carrier domain is shown in Figure S1A, Supporting Information along with the axis of rotation that was set to be the carrier symmetry line. The carrier was modeled as a rigid body. Stationary cylindrical fluid domains were built around the carrier to capture the interaction between the rotating carrier and the surrounding fluid, which is displayed in Figure S1B,C, Supporting Information. The diameter of the surrounding domains is big enough for the outer layer to be beyond the boundary layer. The main variables in the simulations were the rotational frequency (0.25–6 Hz) and cavity diameter (0.1–5 mm), which were systematically varied to investigate their impact on fluid exchange within the cavity.

Before progressing with the analysis, appropriate simulation settings had to be identified. First, laminar flow module was used within COMSOL framework to conduct fluidics simulations. As mentioned, looking at the graphs of fluid flow inside the cavity when the carrier rotates at different frequencies in Figure 2A–C, vortex generation is evident, which can be an indicator of turbulence. Therefore, to characterize the flow, we calculated Reynolds number *Re* as well as Taylor *Ta* and Rossby *Ro* numbers. It was then concluded that there is a laminar flow with vortices given the desired carrier dimensions (8 mm in diameter, 12 mm in length): $Re < 100$, $Ta > 1700$, $Ro < 0.5$.[39] Therefore, the laminar flow physics was an appropriate choice. Next, we put two boundary probes on the interface between the cavity and outer volume shown in Figure S1D, Supporting Information to quantify the fluid exchange. Since V_{out} must be equal to V_{in} across the same boundary, their difference was used as an error criterion to tune the simulation settings and perform mesh convergence analysis. Figure S1E,F, Supporting Information shows the meshed model of the workspace and the carrier.

To verify simulation accuracy and establish an appropriate mesh resolution, we studied the fluid outflow and inflow through the cavity using dedicated probes. The mesh was initially refined until a zero net flow through the cavity was achieved, ensuring mass conservation. Subsequently, the mesh element size was reduced with a step of 10% until we achieved stable outflow results, defined as a relative difference smaller than 0.1% between successive solutions. Regarding time steps, they were set to satisfy Courant–Friedrichs–Lewy stability condition.

We calculated average values of fluid velocity at the cavity interface after the rotating carrier achieves a stable flow profile, which was at most 0.5 s during the analysis, and until the simulation end time, which was set to 2 s.

To calculate the magnetic attraction force F_m generated from the magnetic plate, we used Magnetic Fields, No Current module. Particles were set to be nonmagnetized and made from NdFeB for which B–H curve was found using a vibrating sample magnetometer (VSM EZ7, MicroSense, USA). Simulation settings and resultant mesh body are shown in Figure S1G,H, Supporting Information. Here, a particle (1–50 µm) is placed at a distance (1–8 mm) from the magnetic plate. F_m was set to be equal to F_d, and the latter can be found with Equation (4). Consequently, escape velocity can be found from Equation (5)

$$F_d = \frac{1}{2} C_d \rho_w v^2 A \tag{4}$$

where C_d is a drag coefficient set to 1.17 (2D circular shape), ρ_w is the density of the medium, i.e., water that is equal to 1000 kg m^{-3}, v is the velocity of the particle, and A is the cross-sectional area of the particle equal to $\pi d_{particle}^2/4$.

$$v_{escape} = \sqrt{\frac{2 F_m}{C_d \rho_w A}} \tag{5}$$

Magnetic Cap Characterization: To characterize the magnetic cap opening, the MSC was placed in a water-filled Plexiglas cubic container under a uniform magnetic field generated by the OctoMag system (MagnebotiX, Switzerland), Figure S4, Supporting Information. The magnetic field was controlled within a range of 0 to 80 mT, and an optical image of the opening angle was captured at each 5 mT increment. The opening angle was measured geometrically from the captured images, defined as the angular span between the front face of the MSC and the line tangent to the tip of the cap. For both the Dragonskin and Ecoflex composite caps, five different samples were tested, and the measurements shown in Figure 3C represent the mean values obtained from these samples.

The mechanical properties of the Ecoflex and Dragonskin caps were characterized by using a universal testing machine (INSTRON 5965, USA). Cyclic tensile tests were conducted on standardized samples to obtain stress-strain curves, from which the Young's modulus was determined. Magnetic remanence was measured using the vibrating sample magnetometer. To simulate the cap opening at large angles, we added in Equation (3) a nonlinear phenomenological law

$$T_e(\theta) = k\theta + c_3\theta^3 \tag{6}$$

(where c_3 is obtained by quasistatic calibration) and solved the resulting torque balance numerically.

Release Experiments: Release tests were performed to quantitatively assess the amount of particles released by the carrier in different configurations. The tests were performed using the OctoMag system to manipulate the carrier. The MSC was immersed in a Plexiglas cubic container filled with 10 mL of deionized water, which was positioned at the center of the OctoMag workspace. For each measurement, the internal cavity of the carrier was loaded with 10 mg of 5 µm NdFeB particles dispersed in 15 µL of deionized water. A rotating magnetic field of constant magnitude of 60 mT was applied to actuate the carrier and to ensure an optimal cap opening for release.

To measure the magnetic particles released by the carrier, we first collected the solution of particles and water present in the cubic container and then studied the absorbance spectrum of the solution using a LAMBDA 45 UV–vis spectrophotometer (PerkinElmer, USA). A specific absorbance value corresponds to a particular concentration of magnetic particles. By measuring the absorbances for different known concentrations of magnetic particles, we built a calibration line (Figure S6, Supporting Information). Then, inferencing on the collected absorbance data, we obtained the particle concentration for each release event. The release efficiency was determined by comparing the release concentration to a reference concentration value corresponding to the complete release of the particle initially stored in the cavity.

Locomotion Control and Analysis: The carrier was controlled using a permanent magnet (N42, 60 × 70 × 10 mm, HKCM Engineering, Germany) mounted on a robotic arm (Melfa RV-3SB, Mitsubishi), as shown in Figure S5, Supporting Information. The robotic arm features a terminal joint with passive rotational freedom, resulting in a system with five degrees of freedom (5-DOF), which can be teleoperated using a joystick.

The carrier trajectory during the floating locomotion was first recorded optically by a camera (Sony Alpha 6400) and then calculated using the software Tracker.[40] For each proposed path, three trials were conducted, and the average deviation from the mean trajectory was calculated.

The measurements presented in Figure 5G were obtained by placing the MSC, either loaded or empty, in a petri dish (15 cm in diameter) filled with water or glycerol. The translational rolling velocities at various actuation frequencies were determined by measuring the time required for the carrier to travel along a straight 10 cm path and dividing this distance by the recorded time.

Particle loss during locomotion (floating and rolling) was evaluated by navigating the carrier in the 15 cm diameter petri dish filled with deionized water. For floating locomotion, the MSC was propelled at a velocity of 40 mm s^{-1} under an applied magnetic field of 2 mT. Rolling locomotion was performed at a frequency of 1 Hz with an applied field of 5 mT.

The minimal magnetic gradient necessary to overcome static friction and initiate motion inside a tube was quantified by gradually increasing the distance between the carrier and the external magnet with a step of 1 mm, until the point of detachment and loss of magnetic link was reached. A 3D Hall effect magnetic sensor with 0.13 mT sensitivity (TLE493D-W2B6, Infineon Technologies, Germany) was used to measure the magnetic field at the different distances, and then magnetic gradients were derived.

Supporting Information

Supporting Information is available from the Wiley Online Library or from the author.

Acknowledgements

This work was supported by the European Commission under the Horizon Europe program (REGO Project, Grant #101070066).

Open access publishing facilitated by Scuola Superiore Sant'Anna, as part of the Wiley - CRUI-CARE agreement.

Conflict of Interest

The authors declare no conflict of interest.

Data Availability Statement

The data that support the findings of this study are available from the corresponding author upon reasonable request.

Keywords

magnetic capsule robot, magnetic control, particle release, small-scale robotics, targeted drug delivery

Received: August 4, 2025
Revised: November 13, 2025
Published online: January 6, 2026

[1] H. Rosen, T. Abribat, *Nat Rev Drug Discov.*, **2005**, *4*, 381.
[2] A. S. Lübbe, C. Alexiou, C. Bergemann, *J. Surg. Res.* **2001**, *95*, 200.
[3] A. Vikram Singh, M. Sitti, *CPD* **2016**, *22*, 1418.

[4] D. Liu, T. Wang, Y. Lu, *Adv. Healthcare Mater.* **2022**, *11*, 2102253.
[5] B. J. Nelson, I. K. Kaliakatsos, J. J. Abbott, *Annu. Rev. Biomed. Eng.* **2010**, *12*, 55.
[6] N. Ebrahimi, C. Bi, D. J. Cappelleri, G. Ciuti, A. T. Conn, D. Faivre, N. Habibi, A. Hošovský, V. Iacovacci, I. S. M. Khalil, V. Magdanz, S. Misra, C. Pawashe, R. Rashidifar, P. E. D. Soto-Rodriguez, Z. Fekete, A. Jafari, *Adv. Funct. Mater.* **2021**, *31*, 2005137.
[7] H. Zhou, C. C. Mayorga-Martinez, S. Pané, L. Zhang, M. Pumera, *Chem. Rev.* **2021**, *121*, 4999.
[8] W. Hu, G. Z. Lum, M. Mastrangeli, M. Sitti, *Nature* **2018**, *554*, 81.
[9] Z. Yang, L. Zhang, *Adv. Intell. Syst.* **2020**, *2*, 2000082.
[10] Y. P. Lai, T. Lee, D. Sieben, L. Gauthier, J. Nam, E. Diller, *IEEE Trans. Biomed. Eng.* **2024**, *71*, 2911.
[11] N. K. Mandsberg, G. Moro, M. Ghavami, S. B. Andersen, E. Nedergaard de Visser, M. F. Bertelsen, M. S. Mortensen, T. R. Licht, A. Boisen, *Adv. Mater. Technol.* **2024**, *17*, 2400434, https://doi.org/10.1002/admt.202400434.
[12] K. Kim, S. Edwards, K. Fuxa, H. Lin, S. Shrestha, H. Fan, N. Diaz, J. Berinstein, R. Naik, Y. Zhou, X. Dong, *Adv. Mater. Technol.* **2025**, *10*, 2401487.
[13] Z. Yang, C. Xu, J. X. Lee, G. Z. Lum, *Adv. Mater.* **2024**, *36*, 2408750.
[14] Y. Wang, J. Shen, S. Handschuh-Wang, M. Qiu, S. Du, B. Wang, *ACS Nano* **2023**, *17*, 27.
[15] R. Mundaca-Uribe, E. Karshalev, B. Esteban-Fernández de Ávila, X. Wei, B. Nguyen, I. Litvan, R. H. Fang, L. Zhang, J. Wang, *Adv. Sci.* **2021**, *8*, 2100389.
[16] L. Cai, C. Zhao, H. Chen, L. Fan, Y. Zhao, X. Qian, R. Chai, *Adv. Sci.* **2022**, *9*, 2103384.
[17] L. Schwarz, D. D. Karnaushenko, F. Hebenstreit, R. Naumann, O. G. Schmidt, M. Medina-Sánchez, *Adv. Sci.* **2020**, *7*, 2000843.
[18] J. Li, B. Esteban-Fernández de Ávila, W. Gao, L. Zhang, J. Wang, *Sci. Robot* **2017**, *2*, eaam6431.
[19] M. Shinkai, A. Ito, *Recent Progress of Biochemical and Biomedical Engineering in Japan II*, in Advances in Biochemical Engineering/ Biotechnology, Vol. *91*, Springer Berlin Heidelberg, BerlinHeidelberg **2004**, pp. 191–220.
[20] M. Arruebo, R. Fernández-Pacheco, M. R. Ibarra, J. Santamaría, *Nano Today* **2007**, *2*, 22.
[21] B. Thiesen, A. Jordan, *Int. J. Hyperthermia* **2008**, *24*, 467.
[22] D. Horák, M. Babič, H. Macková, M. J. Beneš, *J. Separation Sci.* **2007**, *30*, 1751.
[23] Y. Chen, Z. Xu, Q. Xu, *Cell Rep. Phys. Sci.* **2024**, *5*, 102059.
[24] T. Srymbetov, G. De Angelis, A. Menciassi, V. Iacovacci, in *2024 10th IEEE RAS/EMBS Inter. Conf. for Biomedical Robotics and Biomechatronics (BioRob)*, IEEE, Heidelberg, Germany **2024**, pp. 985–990.
[25] Z. Xu, Z. Wu, M. Yuan, Y. Chen, W. Ge, Q. Xu, *iScience* **2023**, *26*, 106727.
[26] L. Zheng, S. Guo, M. Kawanishi, *IEEE Syst. J.* **2022**, *16*, 6413.
[27] Z. Cai, Y. Qin, J. Han, *IEEE Trans. Ind. Electron.* **2024**, *71*, 9150.
[28] J. Sikorski, C. M. Heunis, R. Obeid, V. K. Venkiteswaran, S. Misra, *IEEE Trans. Robot.* **2022**, *38*, 1959.
[29] H. Torlakcik, S. Sevim, P. Alves, M. Mattmann, J. Llacer-Wintle, M. Pinto, R. Moreira, A. D. Flouris, F. C. Landers, X.-Z. Chen, J. Puigmartí-Luis, Q. Boehler, T. S. Mayor, M. Kim, B. J. Nelson, S. Pané, *Adv. Sci.* **2024**, *11*, 2404061.
[30] A. Joshi, R. Chaudhari, R. D. Jayant, *Advances in Personalized Nanotherapeutics* (Eds: A. Kaushik, R. D. Jayant, M. Nair), Springer International Publishing, Cham **2017**, pp. 131–156.
[31] U.S. Food and Drug Administration, "Size, shape, and other physical attributes of generic tablets and capsules," U.S. Food and Drug Administration, Guidance for Industry,Oct. **2022**. [Online]. Available: https://www.fda.gov/regulatory-information/search-fda-guidance-documents/size-shape-and-other-physical-attributes-generic-tablets-and-capsules.
[32] P. N. Shankar, M. D. Deshpande, *Annu. Rev. Fluid Mech.* **2000**, *32*, 93.
[33] P. R. N. Childs, *Rotating Flow*, Oxford, UK, (Elsevier **2011**), pp. 249–298.
[34] R. Hong, M. J. Cima, R. Weissleder, L. Josephson, *Mag. Resonance in Med.* **2008**, *59*, 515.
[35] R. Zhao, Y. Kim, S. A. Chester, P. Sharma, X. Zhao, *J. Mech. Phys. Solids* **2019**, *124*, 244.
[36] X. Li, W. Yu, J. Liu, X. Zhu, H. Wang, X. Sun, J. Liu, H. Yuan, *Int. J. Solids Struct.* **2023**, *279*, 112344.
[37] E. M. Stewart, L. Anand, *J. Mech. Phys. Solids* **2025**, *194*, 105934.
[38] Z. Chen, H. Ren, W. Fan, P. Zhou, *Nonlinear Dyn.* **2025**, *113*, 6157.
[39] R. Ostilla-Mónico, S. G. Huisman, T. J. G. Jannink, D. P. M. Van Gils, R. Verzicco, S. Grossmann, C. Sun, D. Lohse, *J. Fluid Mech.* **2014**, *747*, 1.
[40] D. Brown, presented at *AAPT Summer Meeting* , Edomonton, Alberta, July **2008**. https://www.compadre.org/osp/items/detail.cfm?ID=7844.